

Predictability of Tropical Rainfall and Waves: Estimates from Observational Data

Ying Li^{1*} | Samuel N. Stechmann^{1*, 2*}

¹Department of Mathematics, University of Wisconsin-Madison, Madison, WI, 53706, USA

²Department of Atmospheric and Oceanic Sciences, University of Wisconsin-Madison, Madison, WI, 53706, USA

Correspondence

Ying Li, Department of Mathematics, University of Wisconsin-Madison, Madison, WI, 53706, USA
Email: li526@wisc.edu

Funding information

Submitted on July 28, 2019
Revised on December 27, 2019

For tropical rainfall, there are several potential sources of predictability, including synoptic-scale convectively coupled equatorial waves (CCEWs) and intraseasonal oscillations such as the Madden–Julian Oscillation (MJO). In prior work, predictability of these waves and rainfall has mainly been explored using forecast model data. Here the goal is to estimate the intrinsic predictability using, instead, mainly observational data. To accomplish this, Tropical Rainfall Measuring Mission (TRMM) data is decomposed into different wave types using spectral/Fourier filtering. Predictability of MJO rainfall is estimated to be 22 to 31 days, depending on longitude, as measured by the lead time when pattern correlation skill drops below 0.5. Predictability of rainfall associated with convectively coupled equatorial Rossby waves, Kelvin waves, and a background spectrum or non-wave component are estimated to be 8 to 12 days, 2 to 3 days and 0 to 3 days, respectively. Combining all wave types, the overall predictability of tropical rainfall is estimated to be 3 to 6 days, over the Indian and Pacific Ocean regions, and on equatorial synoptic and planetary length scales. For comparison, outgoing longwave radiation (OLR) was more predictable than rainfall by 5 to 10 days over these regions. Wave-removal tests were also conducted to estimate the contribution of each wave type to the overall predictability of rainfall. In

* Equally contributing authors.

summary, no single wave type dominates the predictability of tropical rainfall; each of the types (MJO, CCEWs, and non-wave component) has an appreciable contribution, due to variance contribution, length of decorrelation time, or a combination of these factors.

KEYWORDS

Predictability, Tropical Rainfall, MJO, CCEWs

1 Introduction

Different types of “weather waves” exist in different areas of the globe. While baroclinic eddies generate much of the synoptic-scale weather fluctuations in midlatitudes, convectively coupled equatorial waves (CCEWs) are, in a sense, the “weather waves” of the tropics. CCEWs are a significant component of synoptic-scale variability—i.e., time scales of roughly 2–10 days and length scales of roughly 1,000–10,000 km (e.g., [Takayabu, 1994a,b](#); [Wheeler and Kiladis, 1999](#); [Kiladis et al., 2009](#)). The Madden–Julian Oscillation (MJO) is another significant contributor to tropical weather and climate, with a larger-scale signature on scales of roughly 30–90 days and 20,000 km (e.g., [Zhang, 2005](#); [Lau and Waliser, 2012](#); [Waliser, 2012](#)).

In the present paper, some of the main questions of interest are: What are the intrinsic limits of predictability of the “weather waves” of the tropics (CCEWs and the MJO)? Furthermore, to what extent do CCEWs and the MJO contribute to predictability of, more generally, tropical rainfall? The goal is to estimate both (i) the predictability of wave signals of each individual type and (ii) the predictability of the overall precipitation signal, which is comprised of a mixture of the signals of different waves and a “background” signal ([Wheeler and Kiladis, 1999](#); [Hottovy and Stechmann, 2015](#)). If the “background signal” is overwhelmingly strong, then the CCEWs may not contribute much predictability to the overall precipitation signal; on the other hand, it is also possible that the coherence of CCEWs may contribute to an enhancement in the amount of predictability of tropical precipitation, beyond the predictability of the “background signal” alone.

An investigation of these questions serves many purposes. For instance, CCEWs and the MJO have been difficult to simulate in global climate models (e.g., [Lin et al., 2006](#); [Hung et al., 2013](#); [Jiang et al., 2015](#)); and for assessing model performance, forecast skill could be a useful metric if upper bounds on predictability are known (e.g., for the MJO, see [Waliser, 2012](#); [Neena et al., 2014](#)). Also, if CCEWs are shown to offer a significant source of predictability, then it would provide motivation for the search for improved understanding and simulation of CCEWs.

Some recent work has provided some estimates of the predictability of CCEWs and tropical precipitation, and the approach of the present paper will differ in many ways. [Ying and Zhang \(2017\)](#) investigated predictability using convection-permitting simulations with the Weather Research and Forecasting (WRF) model. The 9-km horizontal grid spacing provided detailed simulations of multi-scale tropical weather systems, although it was computationally expensive and the investigation was limited to approximately one month. [Dias et al. \(2018\)](#) and [Janiga et al. \(2018\)](#) investigated larger amounts of data from approximately one year and over five years, respectively. These latter two studies used data from several numerical weather predictions models such as the Global Forecast System (GFS) of the National Centers for Environmental Prediction (NCEP), the Integrated Forecast System (IFS) of the European Centre for Medium-Range Weather Forecasts (ECMWF), the NCEP Climate Forecast System, version 2 (CFSv2), and the Navy Earth System Model (NESM). In the present paper, in contrast, predictability will be estimated without a numerical weather prediction model; instead, estimates of predictability will be derived from primarily observational data. As such,

these different approaches provide complementary estimates that together can give a fuller picture of predictability. Some of the advantageous aspects of the present approach are that (i) the use of mainly observational data provides perhaps a more independent estimate, since it is not subject to the particulars of physics assumptions within models, and (ii) the computational expense of the model simulations is eliminated, which allows us to consider relatively long time series with relatively little computational expense.

The concept of predictability can be categorized into intrinsic predictability versus practical predictability. Intrinsic predictability represents the inherent limit of prediction given a nearly perfect forecast model of dynamical system and nearly perfect initial/boundary conditions; in such a setting, the predictability is then an indication of the chaotic nature of the dynamical system (Lorenz, 1969; Zhang and Epifanio, 2007; Sun and Zhang, 2016). Practical predictability is the ability to make a prediction, given realistic uncertainties in both the forecast model and initial/boundary conditions (Lorenz, 1982, 1996; Zhang and Nielsen-Gammon, 2006). The prior work of Dias et al. (2018) and Janiga et al. (2018) was mainly related to practical predictability. In the present paper, the approach is perhaps more closely aligned with estimating intrinsic predictability, since perfect initial conditions are used, and since the results do not rely on a numerical weather prediction model.

The remainder of the paper is organized as follows. In section 2, the observational data is described, along with the methods for estimating predictability. In section 3, estimates of predictability are presented for the rainfall associated with individual wave types (MJO, CCEWs, and the non-wave component). In section 4, the different wave types are combined to provide estimates of predictability of the full rainfall signal. In section 5, the predictability of rainfall data is compared with the predictability of outgoing longwave radiation (OLR) data. Finally, section 7 includes a concluding discussion.

2 Data and Methods

2.1 Data and Setup

The Tropical Rainfall Measuring Mission (TRMM) data is used here for investigating the intrinsic predictability. The TRMM data mainly used in this paper has a daily temporal resolution and 0.25° spatial resolution running from January 1st, 1998 to December 31st, 2017. Daily precipitation totals are derived from 3B42 Research Version. The dataset is downloaded from <https://pmm.nasa.gov/data-access/downloads/trmm>.

TRMM data is available at different temporal resolution including the 3 hourly product and the daily product. While the 3-hourly data comes with the advantage of higher temporal resolution, it also has some disadvantages. For instance, the 3-hourly data will include the diurnal cycle, which may a priori need some special treatment, and 3-hourly data is perhaps not necessary for investigating the wave types with the largest spectral peaks (MJO, Kelvin, and Rossby Wheeler and Kiladis, 1999). For this reason, the daily version of TRMM data is mainly used here unless otherwise specified. Some sensitivity tests using 3-hourly data and further discussions are included in section 6.

For testing the robustness and sensitivity of the main results, in addition to TRMM precipitation data, gridded daily interpolated OLR data from January 1979 to December 2013 from National Oceanic and Atmospheric Administration (NOAA) polar-orbiting satellites are also analyzed in this study. OLR data has often been used in the past as a proxy for tropical precipitation and deep tropical convection, so it is interesting to compare the predictability of OLR with the predictability of TRMM data (OLR download link: https://www.esrl.noaa.gov/psd/data/gridded/data.interp_OLR.html). The OLR data initially from NCAR archives has gaps, and the gaps have been filled using temporal and spatial interpolation (Liebmann and Smith (1996)) to create the interpolated OLR data used here. The data for each day are archived on a resolution of 2.5° latitude \times 2.5° longitude globally. Note that the OLR and TRMM datasets have different

native resolutions; therefore, in making comparisons between the two, a spatial filter is used to include only certain wavelengths that are resolved by both datasets; see section 5 for the specifications.

For the purpose of assessing model parameters and evaluating the prediction skills, the dataset is split into training data and testing data. The long time data before the year 2011 for TRMM (the year 2005 for OLR) is used as the training period for training parameters in the model and January 2011 to December 2015 (January 2005 to December 2009 for OLR) serves as the prediction period for testing. Data after the year 2015 is not used as testing data since a cosine tapering has been applied for these data for the purpose of Fourier transform. In the preprocessing, a smoothed seasonal cycle of the entire dataset is removed via the annual mean and the first three harmonics for all the data, so the remaining data represent anomalies from the seasonal cycle. An alternative definition of the seasonal cycle was also tested, where the hard cut-off at the third harmonic was replaced by a smoothed cutoff defined by a cosine tapering, and no significant differences in the results were seen.

CCEWs have a meridional structure with equatorial synoptic length scale of $O(1000)$ km (e.g., Kiladis et al., 2009; Ogrosky and Stechmann, 2016). For this reason, instead of taking data at all the spatial and temporal points directly, we are only considering rainfall after averaging over the tropical belt, which provides a rainfall signal $r(x, t)$ for longitude x and time t . In the future it would be interesting to consider the rainfall signal at each latitude y instead of averaging over the tropical belt. The tropical belt average is performed with a Gaussian weight, which can be viewed as a projection onto a parabolic cylinder function. Specifically, the projection to parabolic cylinder mode 0 is used here, namely projecting the data onto the function

$$\phi_0(y) = \frac{1}{\pi^{1/4}} e^{-y^2/2}. \quad (1)$$

To define the projection, denote $r(x, y, t)$ as the rainfall data, where x is the longitude, y is the latitude, and t is the time. In (1), y is nondimensional, created by scaling with the reference scale 1500km. The discrete version of tropical belt average (the projection) then is

$$r(x, t) = \int_{-\infty}^{\infty} r(x, y, t) \phi_0(y) dy \approx \sum_{90^\circ S}^{90^\circ N} r(x, y_i, t) \phi_0(y_i) \Delta y \quad (2)$$

While it is also common to instead average with equal weight over a band of latitudes such as $10^\circ S$ to $10^\circ N$, the Gaussian weight is chosen here because it provides a smoother average, and it provides a connection with the parabolic cylinder functions, which provide a set of meridional basis functions for equatorial waves. Averaging meridionally using a Gaussian weight is also used in some previous papers (e.g., Stechmann and Ogrosky, 2014; Stechmann and Majda, 2015; Ogrosky and Stechmann, 2016; Ogrosky et al., 2017). Note that for some wave types, such as equatorial Rossby waves, an even tighter connection with equatorial wave theory would perhaps use additional parabolic cylinder functions, since the convergence patterns of equatorial Rossby waves include off-equatorial contributions. Also note that, by using a symmetric-in- y average in (1)–(2), the data is not expected to include the mixed Rossby–gravity (MRG) waves, since their signal appears in the antisymmetric data (i.e., the data from equator-to- $5^\circ N$ -averaged precipitation, minus equator-to- $5^\circ S$ -averaged precipitation; Wheeler and Kiladis, 1999). While the symmetric-in- y data from (1)–(2) will be the main focus here, the methods have also been repeated for antisymmetric-in- y data by replacing $\phi_0(y)$ in (1)–(2) with $\phi_1(y) = \pi^{-1/4} \sqrt{2} y \exp(-y^2/2)$. Using $\phi_1(y)$ instead of $\phi_0(y)$ allows the antisymmetric-in- y data to be identified, and it is used in the results below to investigate the predictability of MRG and $n = 0$ eastward inertio-gravity (EIG) waves.

2.2 Wave Decompositions with Fourier Filtering

For identifying signals due to different types of waves, the main method used in this study is the space-time spectral analysis (e.g., [Wheeler and Kiladis, 1999](#)). A brief overview is as follows.

The method begins with some preprocessing, described above, to remove the seasonal cycle, and to obtain an average over the latitudes near the equator, via a Gaussian weight. The result of the preprocessing is $r(x, t)$, from (2). As further pre-processing, a cosine tapering is applied near the beginning and end of the time series, so the values of the time series are zero at the beginning and end, thereby providing a signal that is periodic in time, in preparation for a Fourier Transform.

Next, a spatial Fourier Transform followed by a temporal Fourier Transform is applied on the longitude-time data $r(x, t)$ to convert the signal into the wavenumber–frequency domain, namely,

$$r(x, t) = \sum_k \sum_{\omega} \hat{r}_{k,\omega} e^{-i\omega t} e^{2\pi i k x / P_e}, \quad (3)$$

where k is the zonal wavenumber, ω is the frequency and P_e is the circumference of the Earth at the equator (approximately 40,000 km). The Fourier coefficients $\hat{r}_{k,\omega}$ are then used to identify the different wave types.

In order to isolate the signal for each of the different wave types (e.g., MJO, CCEWs, etc.), we follow the method of Fig. 6 of [Wheeler and Kiladis \(1999\)](#). In particular, each wavenumber–frequency point (k, ω) is assigned to a different wave type α , where α is an index that indicates the wave type (MJO, Kelvin, Equatorial Rossby, and the non-wave component). The Fourier decomposition in Eqn. 3 can then be written as a sum over different wave types α , rather than a sum over different frequencies ω :

$$r(x, t) = \sum_k \sum_{\alpha} \hat{r}_{k,\alpha}(t) e^{2\pi i k x / P_e}, \quad (4)$$

with

$$\hat{r}_{k,\alpha}(t) = \sum_{\omega \in \Omega_{k,\alpha}} \hat{r}_{k,\omega} e^{-i\omega t}, \quad (5)$$

where α is an index that indicates the wave type (MJO, Kelvin, Equatorial Rossby, and the non-wave component) and $\Omega_{k,\alpha}$ is the set of frequencies for wave type α at wavenumber k .

For example, for the MJO, $\Omega_{k,\alpha}$ is set to be $\Omega_{k,\alpha} = \{\omega : 1/96 \leq \omega \leq 1/30\}$ for wavenumber $k = 1, 2, 3, 4, 5$ to extract MJO signals $\hat{r}_{k,\alpha}(t)$ via Eqn. 5 at wavenumber $k = 1, 2, 3, 4, 5$. In practice, the dataset is filtered to keep the part from 1/96 cpd to 1/30 cpd in the wavenumber-frequency domain for wavenumber $k = 1, 2, 3, 4, 5$ respectively and set all the other part of the data for wavenumber $k = 1, 2, 3, 4, 5$ all zeros. To convert back, an inverse Fourier transform is applied to the filtered data for each wavenumber k from 1 to 5. After that, the first 10% and the last 10% of these data at each wavenumber are cut (due to the cosine tapering applied at the beginning and end of the dataset to facilitate the Fourier transform). Then predictions are made using these filtered data at each wavenumbers independently. The total true MJO signal is considered to be the combination of these final filtered data for wavenumber $k = 1, 2, 3, 4, 5$ (i.e., $\sum_{k=1}^5 \hat{r}_{k,\alpha}(t) e^{2\pi i k x / P_e}$) and the prediction for the total MJO signal is generated by combining predictions at each wavenumber in the same way (i.e., $\sum_{k=1}^5 \hat{r}_{k,\alpha}^{pred}(t) e^{2\pi i k x / P_e}$, where $\hat{r}_{k,\alpha}^{pred}(t)$ is the prediction for $\hat{r}_{k,\alpha}(t)$). Analyses on other CCEWs (e.g., $n=1$ ER, Kelvin) are performed following the similar procedures by setting a different set to $\Omega_{k,\alpha}$ according to the filtering boxes from Fig. 6 of [Wheeler and Kiladis \(1999\)](#). The “non-wave component” is defined here as

the remaining part of the signal after the MJO, ER, Kelvin waves have been removed from the original spectral data. Westward inertio-gravity (WIG) waves are treated here as a part of the non-wave component, due to the limitations of using daily TRMM observed data, although some explorations of WIG waves with 3-hourly data are described in section 6.

2.3 Modeling Wave Signals as Damped Oscillators with Stochastic Forcing

As motivation for model choice, we recall that a goal here is to estimate predictability with less reliance on operational forecast models and more reliance on observational data. This goal is made possible here by the wave decomposition method described above, since the signal from one individual wave type can be modeled reasonably well by a simple damped oscillator model, which can be used as a simple forecast model. In this section, the simple model is described along with the method for fitting to observational data.

As a simple model for an individual wave type, a damped oscillator with stochastic forcing will be used. Specifically, the complex Ornstein-Uhlenbeck (cOU) process (see, e.g., [Majda and Harlim, 2012](#)) is applied for modeling and predicting filtered signal $\hat{r}_{k,\alpha}(t)$ at each single wavenumber k and each wave type α [recall from (4) the details about defining $\hat{r}_{k,\alpha}(t)$]. The traditional Ornstein-Uhlenbeck process is real-valued and does not oscillate ([Gardiner, 2004](#)); on the other hand, the cOU process is complex-valued and is a damped oscillator with stochastic forcing. The cOU process is also exactly solvable and meaningful for predicting the complex Fourier coefficient $\hat{r}_{k,\alpha}(t)$ for a single wave. In what follows, we write $r(t)$ in place of $\hat{r}_{k,\alpha}(t)$ to simplify notation. The evolution of the cOU process is a complex linear stochastic differential equation:

$$dr(t) = (-\gamma + i\omega)r(t) + \sigma dW(t) \quad (6)$$

where $\gamma, \sigma > 0$ and ω are real numbers and

$$dW(t) \equiv \frac{dW_1(t) + idW_2(t)}{\sqrt{2}} \quad (7)$$

is a complex Gaussian white noise where each component satisfies

$$dW_j(t) \equiv \dot{W}_j(t)dt, \quad j = 1, 2, \quad (8)$$

that is, white noise $\dot{W}_j(t)$ is intuitively like a “derivative” of the Wiener process $W_j(t)$ and it satisfies the following properties:

$$\mathbb{E}[\dot{W}_j(t)] = 0, \quad (9)$$

$$\mathbb{E}[\dot{W}_j(t)\dot{W}_j(s)] = \delta(t - s), \quad (10)$$

$$\mathbb{E}[\dot{W}_i(t)\dot{W}_j(s)] = 0 \quad \text{for } i \neq j. \quad (11)$$

The exact solution of (6) is

$$r(t) = e^{(-\gamma+i\omega)t}r(0) + \sigma \int_0^t e^{(-\gamma+i\omega)(t-s)} dW(s) \quad (12)$$

Here, $1/\gamma$ represents the decorrelation time of the signal and ω is the oscillation frequency with $2\pi/\omega$ to be the time

of one oscillation period. σ is the standard deviation of the white noise. The whole signal $r(t)$ is a periodic decaying signal with random random white noise. As $t \rightarrow \infty$, $r(t)$ will converge to a stationary Gaussian distribution with mean 0 and variance $\sigma^2/(2\gamma)$ (e.g., [Majda and Harlim, 2012](#); [Majda et al., 2001](#)). The autocorrelation function is given by the analytical formula

$$R(\tau) = R(t, t + \tau) = e^{-(\gamma+i\omega)\tau} \quad (13)$$

in the stationary state as $t \rightarrow \infty$ and τ is the lag. To summarize, as a forecast model, (12) provides an ensemble of forecasts, with a forecast mean of $r(t) = e^{(-\gamma+i\omega)t} r(0)$.

One might wonder why white noise is used here, whereas the tropical rainfall spectrum is known to have a form similar to red noise (e.g., [Wheeler and Kiladis, 1999](#); [Hottovy and Stechmann, 2015](#)). The formulation here is, in fact, consistent with a red-noise spectrum of tropical rainfall. The basic feature of spatiotemporal “red noise” is that the variance is decreasing as a function of temporal frequency or spatial wavenumber k . These basic features are actually built into the different values of the parameters γ and σ for different wavenumber k . For instance, for a larger wavenumber k , the fitted cOU process will have a corresponding smaller variance $\sigma^2/2\gamma$ with the fitted values of γ and σ for this particular wavenumber. Different cOU processes are fitted for different wavenumbers independently. With different choices of parameters for different wavenumbers, the basic feature of decreasing variance as a function of wavenumber k is retained.

The model parameters γ, ω are needed to make a forecast, and different values are used for each zonal wavenumber k and wave type α . Here the parameters are chosen by matching the observed autocorrelation of the training data and the analytic autocorrelation function. The model parameters are determined to capture the first maximum/minimum of the real and imaginary parts of the observed autocorrelation for positive lags, except for the non-wave component. For the non-wave component, since it has no propagation direction, its values of ω are nearly zero, so γ, ω are selected by matching the discrete summation of observed autocorrelation function and the integral of the analytic autocorrelation function, a method that provides better model performance. Also, this is consistent with treating the non-wave component like the background spectrum of tropical convection, for which a natural simple model is eddy diffusion ([Hottovy and Stechmann, 2015](#)) without any wave oscillations.

An example of the autocorrelation fitting is shown for the MJO in Figure. 1. The left panel shows the observed autocorrelation function and the analytical autocorrelation function from (13), where the parameters γ and ω were chosen to capture the first maximum/minimum of the real and imaginary parts of the observed autocorrelation function. As seen in the figure, the autocorrelation function of the fitted model has a quite good fitting up to lags of one month, although there is nonnegligible model error for lags that are larger than one month. It is possible that a nonlinear oscillator model (e.g., [Chen et al., 2014](#)) would be able to fit the statistics even more accurately; however, the present paper is aimed at modeling many different wave types and many different wavenumbers, which involves model parameters for each wave type and each wavenumber; therefore, a simple linear oscillator model is advantageous here for its minimal number of parameters, and it provides reasonable results, as shown in Figure. 1.

2.4 Estimating Predictability

To estimate predictability, forecasts are performed using the stochastic, damped oscillator models described in sections 2.2–2.3. The initial conditions $r(0)$ for the forecast are assumed to be perfect, in which case the formula for the

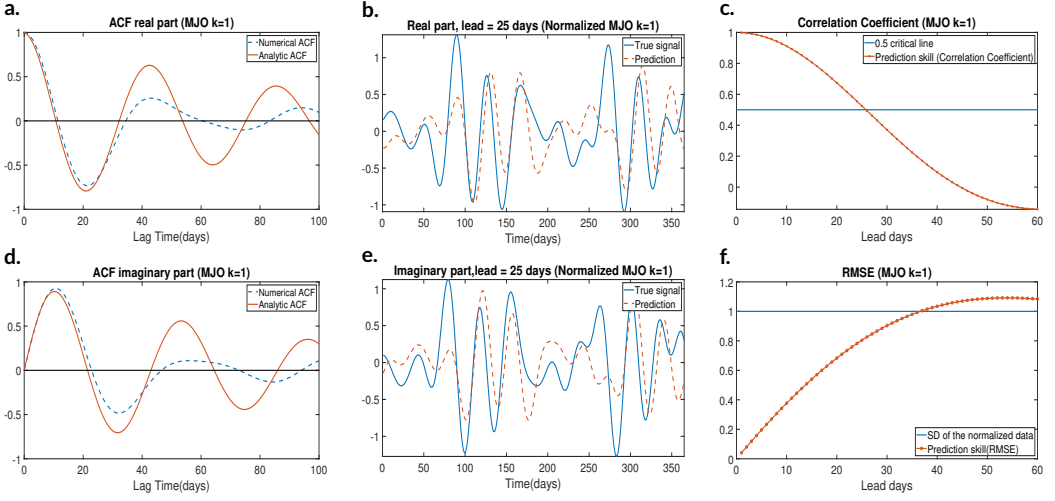


FIGURE 1 Panel a (Panel d): Real (Imaginary) part of the fitted auto-correlation function (red line) and the numerical auto-correlation function from the observational TRMM data (blue line) for wavenumber $k = 1$ of MJO; Panel b (Panel e): Real (Imaginary) part of the time series for MJO ($k=1$) observations and forecasts with lead time as 25 days in the year 2011; Panel c and f: Forecast skill (correlation coefficient and RMSE) for predictions for five-years signals of MJO ($k=1$).

mean prediction is given by the expected value of (12), i.e.,

$$\mathbb{E}[r(t)] = \mathbb{E}[e^{(-\gamma+i\omega)t} r(0) + \sigma \int_0^t e^{(-\gamma+i\omega)(t-s)} dW(s)] = e^{(-\gamma+i\omega)t} r(0). \quad (14)$$

Note that such a forecast method would not be applicable to real-time forecasting due to the use of Fourier filtering in time, as described in section 2.2; some real-time wave decomposition methods have been proposed (e.g., Wheeler and Weickmann, 2001; Wheeler and Hendon, 2004; Kiladis et al., 2014; Stechmann and Ogrosky, 2014; Stechmann and Majda, 2015; Ogrosky and Stechmann, 2015a,b, 2016), although it is not clear that real-time methods are as skillful at wave decompositions as non-real-time methods based on temporal Fourier filtering. In any case, the use of these perfect initial conditions is in line with the main goal here of estimating bounds on intrinsic predictability.

The prediction skill is evaluated by two commonly used criteria, Correlation Coefficient (ρ) and Root Mean Square Error (RMSE). Mathematically, with the true data $\mathbf{X} = (X_1, X_2, \dots, X_N)$ at N points in time and the corresponding predictions $\mathbf{X}^{pred} = (X_1^{pred}, X_2^{pred}, \dots, X_N^{pred})$, the correlation coefficient is calculated by

$$\rho(\mathbf{X}, \mathbf{X}^{pred}) = \frac{\sum_{i=1}^N (X_i - \bar{X})(X_i^{pred} - \bar{X}^{pred})}{\sqrt{\sum_{i=1}^N (X_i - \bar{X})^2} \sqrt{\sum_{i=1}^N (X_i^{pred} - \bar{X}^{pred})^2}} \quad (15)$$

where \bar{X}, \bar{X}^{pred} are the averages of X_i, X_i^{pred} ($i = 1, 2, \dots, N$) respectively and the RMSE is

$$RMSE(\mathbf{X}, \mathbf{X}^{pred}) = \sqrt{\frac{1}{N} \sum_{i=1}^N (X_i - X_i^{pred})^2} \quad (16)$$

The overall forecasting skill is defined as the lead day where $\rho(\mathbf{X}, \mathbf{X}^{pred}) \geq 0.5$ and $RMSE(\mathbf{X}, \mathbf{X}^{pred}) \leq SD(\mathbf{X})$ (standard deviation of the data of the true signal). In other words, the criterion of a reasonable forecast is a threshold of 0.5 for correlation coefficient and 1 standard deviation for the RMSE. These threshold choices are also commonly used in other forecast studies (e.g., [Chen and Majda, 2015](#)).

For the purpose of evaluating cOU predictions and wave exclusion tests, two baselines for comparison are used: the zero prediction and persistence prediction. The zero prediction is obtained by predicting that the signal will be identically zero for all future data points. (Note that the time series is centered to mean zero, so this can also be viewed as a climatological prediction, where the predicted value is the climatological mean.) The persistence prediction is obtained by predicting that the future weather condition will be the same as the present condition.

3 Predictability of Individual Wave Modes: MJO, CCEWs, and the Non-wave Component

In this section, we investigate the question: What is the intrinsic predictability of MJO-related rainfall, CCEW-related rainfall, and background-spectrum rainfall? Each of the wave types will be considered in isolation to identify the predictability of each individual wave mode.

3.1 MJO

MJO predictability is shown for each wavenumber k in [Fig. 2](#) and [Table 1](#). The predictability is defined as the lead time when the correlation coefficient drops to 0.5. In brief, all MJO wavenumbers have predictability of approximately 25–32 days.

As one example forecast for illustration, time series for $k = 1$ are shown in [Fig. 1b,e](#). The figure shows a comparison of the true signal and predicted signal at lead time of 25 days. This lead time was chosen for illustration because it is approximately the predictability limit of the $k = 1$ MJO signal (see [Fig. 2](#) and [Table 1](#)). As seen in [Fig. 1b,e](#), the predicted signal catches the overall variability of the oscillations quite well although it fails to catch the more extreme values with the present simple forecasting framework. In the other panels, in [Fig. 1c,f](#), the RMSE and correlation coefficient are shown. The correlation coefficient is seen to decrease as lead time increases, and it decreases to 0.5 at a lead time of 25 days, which is used as the value reported in [Fig. 2](#) and [Table 1](#).

To move beyond forecasts of individual wavenumbers, we can combine the wavenumbers $k = 1$ to 5 of the MJO signal, using [\(4\)](#). In brief, only the MJO signal (from wave $k = 1$ to 5) is kept, and the signals of all other wave types are set to zero. Algorithmically, the space–time data $r_{MJO}(x, t)$ is then obtained using a temporal inverse Fourier transform followed by a spatial inverse Fourier transform. From the space–time data $r_{MJO}(x, t)$, one can observe a forecast of the MJO at each location around the equator. Such a forecast skill at each longitude is shown in [Fig. 3](#). In terms of RMSE ([Fig. 3 Panel a](#)), the forecast skill is greatest over the Indian Ocean and western Pacific warm pool (longitudes from roughly 60E to 180), although this is also the region of greatest standard deviation in the MJO signal. In terms of correlation coefficient ([Fig. 3 Panel b](#)), the forecast skill is more nearly equal at each longitude. As a summary of forecast skill, in the [Panel c](#) in [Fig. 3](#), it can be seen that the forecast skill is approximately 25–30 days at each longitude, similar to the forecast skill for individual wavenumbers shown in [Fig. 2](#) and [Table 1](#). Hence, whether viewed longitude by longitude or wavenumber by wavenumber, the predictability of the MJO is estimated to be 25–30 days.

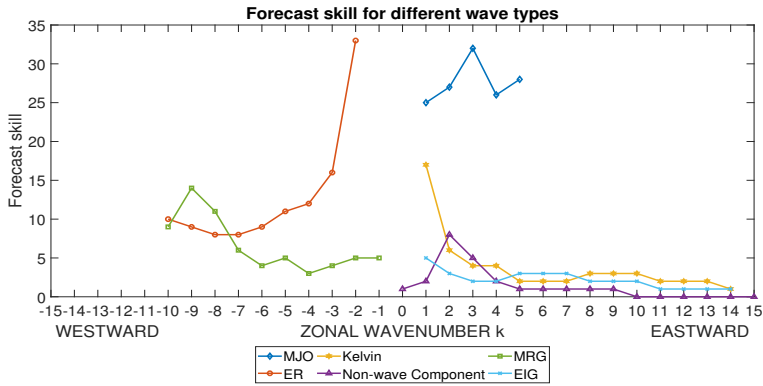


FIGURE 2 Forecast skills for different wavenumbers of MJO, ER wave, Kelvin wave, Non-wave Component, MRG wave and $n = 0$ EIG wave.

Wave type	Wavenumber	Forecast skill [D]	$\gamma[M^{-1}]$	$\omega[2\pi M^{-1}]$	$\hat{\omega}[D^{-1}](CPD)$
MJO	k=1	25	0.33	-4.39	-0.023
MJO	k=2	27	0.37	-4.28	-0.023
MJO	k=3	32	0.36	-4.39	-0.023
MJO	k=4	26	0.35	-4.39	-0.023
MJO	k=5	28	0.41	-4.71	-0.025
ER	k=-2	33	0.17	-6.09	-0.032
ER	k=-3	16	0.52	-7.85	-0.042
ER	k=-4	12	1.03	-9.42	-0.050
ER	k=-5	11	1.08	-11.78	-0.063
ER	k=-6	9	1.18	-12.62	-0.067
Kelvin	k=1	17	0.38	-9.00	-0.048
Kelvin	k=2	6	1.79	-15.71	-0.083
Kelvin	k=3	4	2.85	-23.56	-0.125
Kelvin	k=4	4	3.76	-27.49	-0.146
Kelvin	k=5	2	4.81	-39.27	-0.208
Non-wave Component	k=1	2	1.72	0.08	0.001
Non-wave Component	k=2	8	0.76	-0.20	-0.001
Non-wave Component	k=3	5	1.94	-0.26	-0.001
Non-wave Component	k=4	2	3.52	-0.10	-0.001
Non-wave Component	k=5	1	10.04	-0.29	-0.002
MRG	k=-1	5	1.07	-47.12	-0.250
MRG	k=-2	5	1.29	-47.12	-0.250
MRG	k=-3	4	1.93	-47.12	-0.250
MRG	k=-4	3	2.72	-47.12	-0.250
MRG	k=-5	5	2.21	-39.27	-0.208
EIG	k=1	5	1.30	-47.12	-0.250

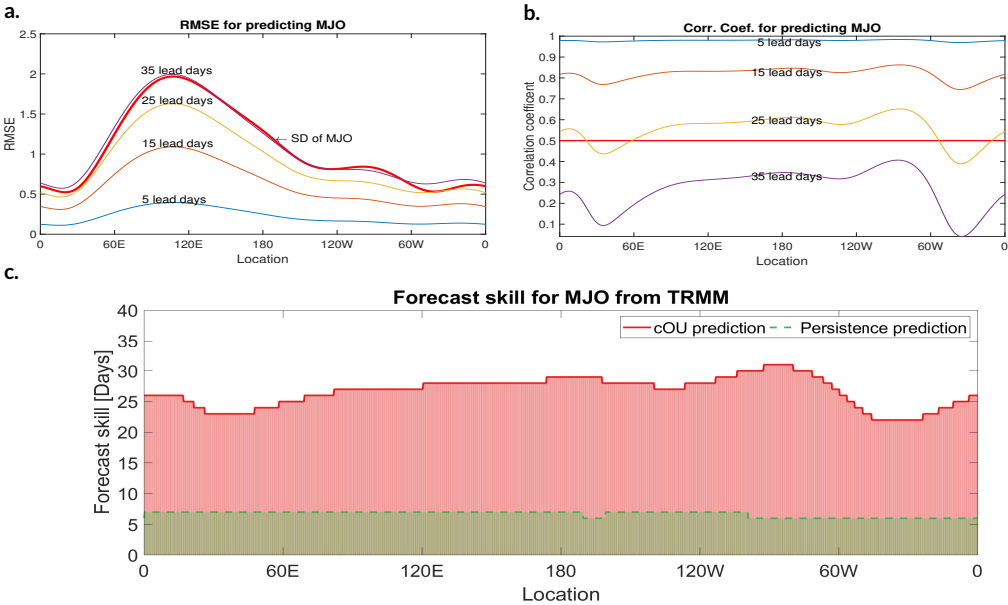


FIGURE 3 Forecast skills for MJO at different locations. Top two panels: RMSE (panel a) and correlation coefficient (panel b) for predicting MJO from TRMM data with different lead days; Bottom panel (panel c): Overall forecast skill for predicting MJO components from TRMM data with different methods cOU (solid pink) and persistence prediction (dashed green).

3.2 CCEWs

Predictability is estimated for two CCEWs: the ER and Kelvin waves. The results will be analyzed from two perspectives: wavenumber by wavenumber, and longitude by longitude.

First, predictability is reported for each individual wavenumber, analyzing each wavenumber separately from each other wavenumber, in Table 1 and Fig. 2. The predictability is seen to depend strongly on wavenumbers. For instance, the ER wave has a predictability of 33 days for wavenumber 1 but a predictability of roughly 8–10 days for wavenumbers 5 to 10; and the Kelvin wave has a predictability of 17 days for wavenumber 1 but a predictability of roughly 2–3 days for wavenumbers 5 to 10. Overall, one can see a rough general trend in Table 1 and Fig. 2: predictability tends to increase as wave oscillation period increases. This is consistent with the intuition that waves with longer oscillation periods also tend to have longer decorrelation time γ^{-1} , and longer decorrelation times are associated with longer predictability times. A figure of $\hat{\omega}$ for different wave types versus different wavenumbers along with some additional figures are also provided in the supporting information.

Second, to analyze the predictability at different longitudes, the data from different wavenumbers are combined together to predict, e.g., the ER signal as a function of longitude. The spatial variations of predictability for the ER and Kelvin waves are shown in the first two columns in Fig. 4. Both ER and Kelvin have their largest variance over the Indian Ocean and western Pacific warm pool, from about 60°E to 150°W. The predictability of the ER wave varies from 8 days to 12 days over all the locations, while the forecast skill of the Kelvin wave varies from 2 days to 3 days, with little variation from location to location.

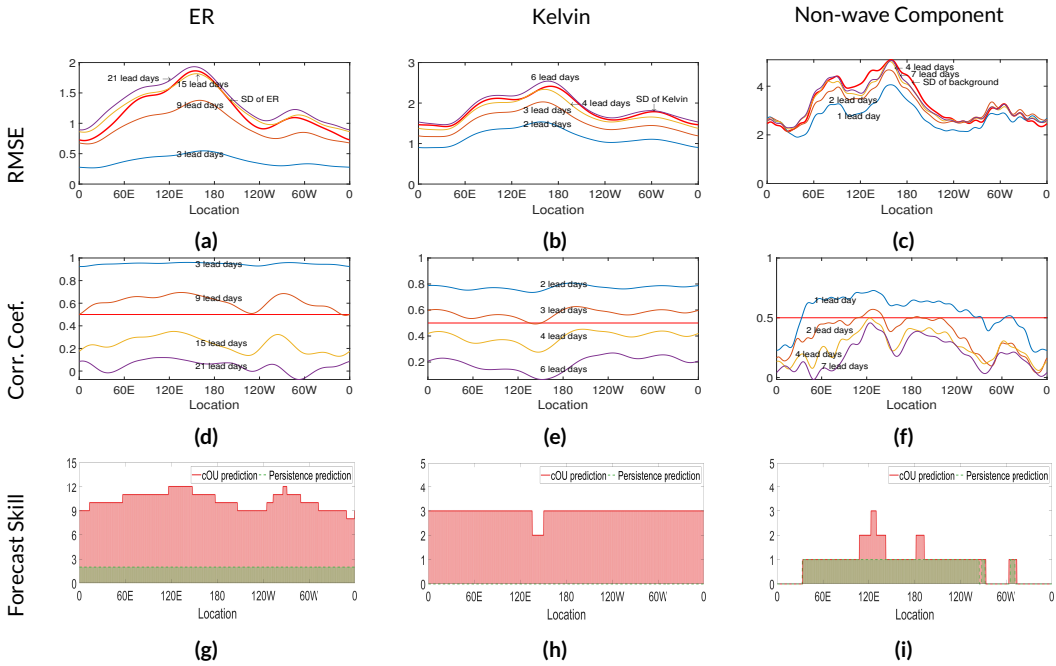


FIGURE 4 Forecast skills for ER wave, Kelvin wave and non-wave component. From the left to right are ER wave (panel a,d,g), Kelvin wave (panel b,e,h) and non-wave component (panel c,f,i), from the top to bottom are RMSE (panel a,b,c), correlation coefficient (panel d,e,f) and overall forecast skill (panel g,h,i).

3.3 Non-wave Component

Lastly, consider the non-wave component. The wavenumber-by-wavenumber results are shown in Table 1 and Fig. 2. Note that the non-wave component is not assigned a particular propagation direction (e.g., eastward or westward), so the $+k$ and $-k$ wavenumbers are analyzed together as a single unit, as wavenumber k . The predictability of the non-wave component is typically low, in the range of 1 to 2 days. An anomaly is seen in wavenumbers 2 and 3, for which the predictability times are 8 and 5 days, respectively; these longer predictability times are likely the result of, e.g., the MJO signal being partially identified as “non-wave component,” since the MJO signal could potentially influence some frequencies that lie outside the filtering box of Fig. 6 of Wheeler and Kiladis (1999). Overall, though, when viewed longitude by longitude (see Fig. 4 Panel (i)), the non-wave component has low predictability of roughly 1 day.

We note here the possibility of localized regions of enhanced predictability, as illustrated by the case of the non-wave component near 120E longitude; see Fig. 4 Panel (i). To ensure that this behavior is not a result of an error in the data analysis, one can trace its source to the plot of correlation coefficients, from which the forecast skill is calculated; see Fig. 4 Panel (f). One can see that the curves for two different lead times (e.g., lead times of 2 and 3 days) can sometimes be nearly overlapping when their correlation coefficients are nearly equal; e.g., see 120E longitude. If this occurs for a correlation coefficient of 0.5 (i.e., the cutoff correlation coefficient for defining the “forecast skill”), then the forecast skill can have a sharp change for nearby longitudes, as seen here for the non-wave component near 120E longitude. Such behavior also appears if OLR data is analyzed instead of TRMM data, as shown below in section 5. We speculate that it may be related to the unique geographical features of the Indo-Pacific maritime continent, such as its associated topography and/or land-sea contrast. This behavior could be eliminated by choosing a different cutoff, such

as 0.6 instead of 0.5, since we see this behavior here for the lower correlation coefficient values of 0.55 or lower; but we will retain the cutoff of 0.5 since it is a commonly used definition of forecast skill.

4 Predictability of Tropical Rainfall

The previous section assessed predictions of rainfall associated with an individual wave type (MJO, ER, Kelvin, or non-wave component). In this section, in contrast, predictions of the full rainfall signal are analyzed. As a first brief look, see Fig. 5. The solid curve indicates the predictability of the full rainfall signal, and it is repeated identically in each panel of the figure. The forecast skill is roughly 3 to 6 days over the Indian and Pacific Ocean regions. This skill represents a substantial improvement over what was seen for the non-wave component alone (see Fig. 4), which was predictable for only roughly 1 to 2 days. The improved skill can be attributed to the additional wave types beyond the non-wave component: the CCEWs and the MJO.

In what follows, to provide a more detailed view of the full rainfall signal, wave-exclusion studies are also used in order to assess the contribution of each wave type to overall predictability (Sec. 4.1). Also, to assess predictability on different length scales, the planetary length scales (zonal wavenumbers -5 to +5) are investigated in Sec. 4.2.

4.1 Wave-Exclusion Studies

In this section, we ask: How important is each individual wave type for the predictability of the full rainfall signal? To investigate this question, we exclude the predictions of one wave type in predicting TRMM rainfall data, and evaluate the resulting decrease in predictability. To exclude a wave type, two methods are examined: either (i) setting the prediction of the wave's signal to be zero, or (ii) using a persistence prediction for that wave type. While we are changing the predictions for the component of the one wave type of interest, all the other components of the signal are kept being predicted by cOU processes, as in our standard methodology.

The main results of the wave-exclusion studies are shown in Fig. 5. The forecast skill is presented as a function of longitude. With all wave types predicted and none excluded, the precipitation is most predictable over the Indian Ocean to Pacific Ocean regions, where the predictability is roughly 3 to 6 days, aside from the longer predictability of 9 days near 120E. When one wave type is excluded, a substantial loss of predictability is typically seen. In particular, if either the MJO, ER, or non-wave component is excluded, then a loss of predictability of several days can be seen over the Indian Ocean and Pacific Ocean regions.

For the Kelvin wave, on the other hand, the results are somewhat mixed. Little predictability is lost if the Kelvin wave is excluded by predicting it to be zero. Over many parts of the Indian and Pacific Oceans, no predictability is lost, and over other parts of the tropics, the loss is 1 to 2 days of predictability. Given that the overall predictability is only 1 to 2 days for many regions outside the Indian and Pacific Oceans, one could possibly view this as a substantial loss. Also, if the Kelvin wave is instead excluded by using a persistence forecast, then a substantial loss in predictability is seen: roughly 1 to 4 days.

Two factors are perhaps sufficient to explain each wave type's importance: decorrelation time and variance. The decorrelation time (γ^{-1}) has a rough correspondence with the predictability, as seen in Table 1 (see also Figs. 2, 3, and 4). For instance, the MJO and ER waves have the longest decorrelation times and predictability, whereas the non-wave component and Kelvin waves have shorter decorrelation times and predictability. However, decorrelation time alone is not enough to explain the contribution of each wave type to the predictability of overall rainfall. For instance, the MJO and non-wave component have somewhat similar contributions based on the wave exclusion studies (Fig. 5), yet the non-wave component has a very short decorrelation time. Hence, a second factor is needed to explain why the

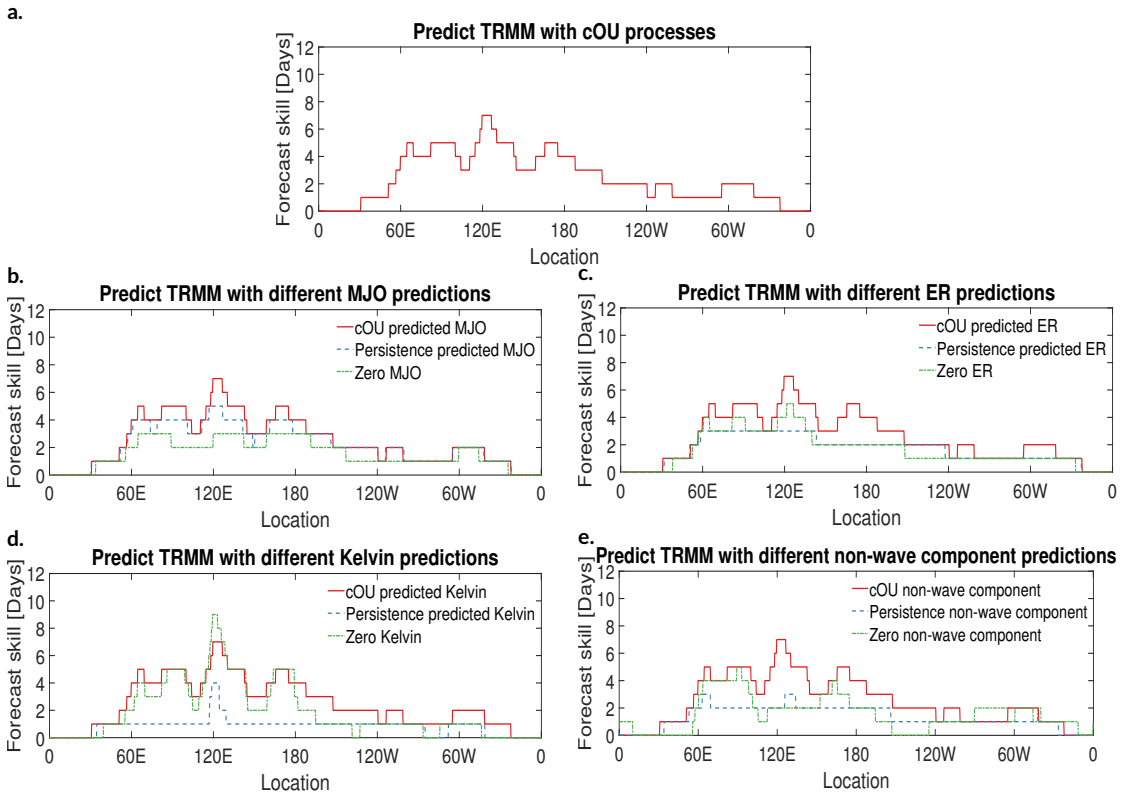


FIGURE 5 Panel a: Forecast skill for predicting TRMM data (wavenumber from -15 to 15) with cOU processes for all wave and non-wave components. Panel b-e: Forecast skills for predicting five-years TRMM data (wavenumber from -15 to 15) with different predicted MJO (Panel b), ER wave (Panel c), Kelvin wave (Panel d) and non-wave component (Panel e). Three forecast methods are used wave-exclusion studies: cOU prediction (pink), persistence prediction (blue) and prediction with all zeros (green).

non-wave component has an important contribution: variance. The variance (or, rather, its square root, the standard deviation) is shown for each wave type in Fig. 6. The non-wave component has the largest standard deviation of all wave types, so substantial predictability will be lost if a poor forecast is used for such a large share of the total standard deviation. In this way, each of the wave types has an appreciable contribution to the overall predictability of rainfall, due to a long decorrelation time or a large variance or a combination of these factors.

4.2 Planetary-Scale Predictions

In the results above, the equatorial synoptic length scales (zonal wavenumbers -15 to +15) were considered, in order to include effects of many CCEWs. Instead, if we are only interested in the large-scale variations of rainfall, is it possible to achieve better prediction skill?

This question is now investigated by considering only zonal wavenumbers $k = -5$ to 5, in order to represent the planetary-scale zonal variations of rainfall. One might expect enhanced predictability if only the largest scales are considered, consistent with the general idea that spatial averaging will improve forecast skill (e.g., [Li and Stechmann](#),

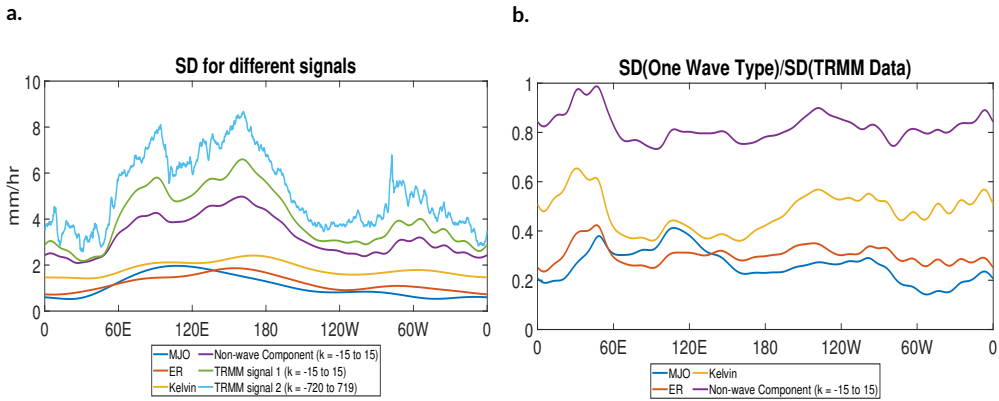


FIGURE 6 Panel a. Standard Deviation (SD) for different signals: MJO, ER, Kelvin, Non-wave component ($k=-15$ to 15), true signal from $k=-15$ to 15 of TRMM data and the original TRMM data (all wavenumbers, from $k=-720$ to $k=719$); Panel b. Standard deviation of the each wave type signal (MJO, ER, Kelvin, Non-wave component) over the standard deviation of the true signal from $k=-15$ to 15 of TRMM data.

2018). Exactly how much improvement is seen? The predictability is shown in Fig. 7. The forecast skill is quite long: roughly 10 to 20 days over the Indian and Pacific Ocean regions. Comparing Fig. 7 to the forecast skills for wavenumbers from -15 to 15 in Fig. 5a, the forecast skill for the planetary scale predictions has very significant improvements from 60°E to 150°W . The planetary scale predictions are overall about 5-15 days more predictable in these areas, particularly near 120°E and 180° with about 10-15 days improvements in forecast skills.

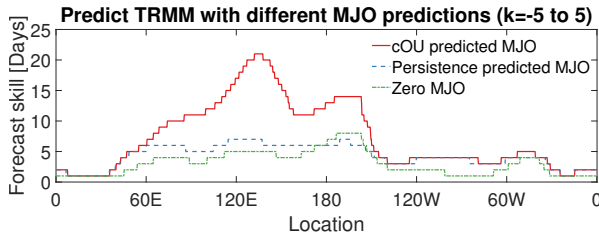


FIGURE 7 Forecast skills for predicting five-years TRMM data on planetary scales (wavenumber from -5 to 5) with different prediction methods for the MJO.

The dominant coherent wave signal on planetary scales is the MJO. How important is the MJO to the predictability of rainfall on planetary scales? To investigate this question, a wave-removal study is implemented where the MJO is removed in one of two different ways: predict the MJO-associated rainfall is zero, or use a persistence prediction for the MJO-associated rainfall. The results are shown in Fig. 7. The forecast skill of tropical rainfall is significantly decreased when the MJO is removed from consideration. Specifically, the forecast skill is only 4 to 7 days over the Indian and Pacific Ocean regions if the MJO is removed. Hence, the MJO plays a crucial role in the predictability of rainfall on planetary scales, and it contributes up to 15 days of additional predictability.

5 Comparing predictability of precipitation versus cloudiness (OLR)

Besides precipitation, another quantitative measure of moist convection is OLR. OLR data is commonly used as a proxy for cloudiness, for many purposes, such as identifying CCEWs or the MJO (e.g., [Wheeler and Hendon, 2004](#); [Kiladis et al., 2014](#)). In prior studies on predictions of CCEWs and the MJO, [Dias et al. \(2018\)](#) analyzed precipitation whereas [Janiga et al. \(2018\)](#) analyzed OLR. The predictability could possibly vary significantly depending on which data is used, since, e.g., OLR and precipitation represent distinct physical quantities with potentially different properties. In this section, we investigate the predictability of OLR, and we compare it with the predictability of precipitation.

For comparing OLR and precipitation, results are shown in [Fig. 8](#), and can be summarized as follows. On the one hand, for the broad conclusions regarding comparisons of different wave types, the results are essentially the same, and they are therefore not repeated in detail for the OLR case. For instance, whether OLR or precipitation data is used, each of the wave types is seen to have an appreciable contribution to the predictability of the full rainfall signal. The detailed amounts of each wave's contribution can be different for OLR versus precipitation, as illustrated in [Fig. 8](#) for the case of the non-wave component (see [section 4](#) for a note about the enhanced predictability of the non-wave component near 120E longitude). Nevertheless, the broad conclusion remains the same: each of the wave types has an appreciable contribution.

On the other hand, one clear difference between OLR and precipitation is that OLR is generally speaking more predictable. [Fig. 8](#) quantifies the difference in predictability. The larger predictability of OLR is seen whether viewing individual wave types or the full rainfall signal. The detailed amount can be different for different wave types; for example, for the non-wave component, [Fig. 8](#) shows that OLR is more predictable than precipitation by only roughly 1 to 2 days at most locations, whereas for the full rainfall signal, OLR is more predictable than precipitation by roughly 5 to 10 days at many locations over the Indian and Pacific Ocean regions. Other wave types, such as the MJO (not shown), are also noticeably more predictable in terms of OLR versus precipitation.

As some additional sensitivity tests, beyond considering two quantities (precipitation and OLR), we also analyzed the impact of using only zonal wavenumbers -15 to 15 in the predictions. In other words, recall that only the synoptic and planetary scales (zonal wavenumbers -15 to 15) have been considered throughout the present paper. Such a choice was made in part because the predictability of wavenumbers with $10 \leq |k| \leq 15$ is already low (see [Table 1](#) and [Fig. 2](#)) and in part because the focus was on CCEWs and the MJO. The predictability of higher wavenumbers ($|k| > 15$) is low, but they could influence the overall predictability if they account for significant variance. To investigate, we now ask the question: If only zonal wavenumbers -15 to 15 are predicted, and if all higher wavenumbers are predicted to be zero, and if the prediction is assessed via comparison with the full dataset (including $|k| > 15$), then what is the resulting prediction skill? In other words, if only wavenumbers -15 to 15 are modeled, how skillfully can the full dataset (including $|k| > 15$) be predicted? The results are shown in [Fig. 8c](#) for the full TRMM rainfall dataset, which includes zonal wavenumbers -720 to 720. The predictability drops significantly, consistent with the fact that the higher wavenumbers (smaller scales) contribute an appreciable amount of variance and tend to be less predictable (e.g., see [Table 1](#) and [Fig. 2](#)). A similar drop in predictability is also seen for OLR in [Fig. 8d](#), although the higher resolution comparison is not too drastically different in its predictability compared to the standard case. OLR predictability may be less sensitive to changes in resolution because it is generally more smoothly varying than precipitation, or possibly because the higher resolution OLR data includes only wavenumbers -72 to 72 (as opposed to the precipitation case which includes wavenumbers -720 to 720 at its highest resolution).

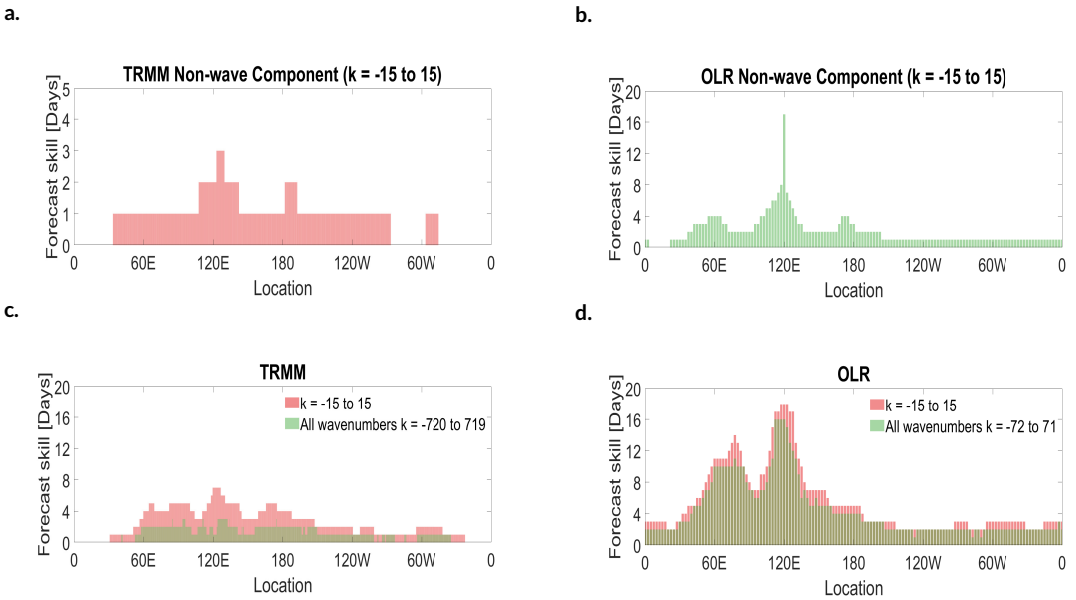


FIGURE 8 Forecast skills for the non-wave component of (a) TRMM and (b) OLR. Forecast skills for the full signal including all wavenumbers for (c) TRMM and (d) OLR. Red bar is for the forecast skill from the comparison between the predictions of 31 wavenumbers and the 31 wavenumbers of the true signal, green bar is for the forecast skill from the comparison between the predictions of 31 wavenumbers and the true signal with all wavenumbers.

6 Discussion

In this section, several additional tests are discussed, along with some additional discussion and comparisons with other studies.

While the results above were obtained using daily data, another version of TRMM rainfall data is also available as 3-hourly data, which offers additional possibilities, such as the resolution of WIG waves. As one test with the 3-hourly data, we compared two cases: one case where WIG waves were treated as its own wave type and another case where WIG waves were included with the non-wave component. In these tests, for each time available in the time series, a 24-hour running time average was used to average over the effects of the diurnal cycle; note that the result is still a 3-hourly time series, although each data point corresponds to a 24-hour time average. In comparing these two cases, the results were essentially the same, suggesting that, at least when analyzed after a 24-hour running time average, the WIG waves do not contribute a substantial addition to the predictability. This is possibly due to the fact that the spectrum is red, so the variance of high-frequency waves such as the WIG waves is a relatively small contribution to the overall rainfall variance and predictability.

Other sensitivity studies were also carried out to examine different ways of modeling the non-wave components. Since the non-wave component has a wide range of frequencies, whereas the CCEW types were defined over more restrictive ranges of wavenumbers and frequencies, one may want to examine alternative methods where the non-wave component is divided into subcomponents. Two alternative cases were considered. First, the non-wave component was divided into the two subcomponents of oscillation periods less than 5 days and greater than 5 days. As a second case, three components were used: periods less than 5 days, between 5 and 10 days, and greater than 10 days. In these

alternative cases, the forecast skill for the non-wave components are nearly the same as in the standard case in Fig. 2 and Table 1. For the different wavenumbers, the skill is either the same as in the standard case, or sometimes 1 day better skill, and 2 days better skill for a small number of wavenumbers. Hence the precise forecast skill of the non-wave component changes a little if different methods are used, but the overall broad conclusions about different wave types still hold.

It is interesting to make some further comparisons with other prior work. For instance, practical and intrinsic predictability of multiscale weather and CCEWs over Indian Ocean were investigated based on the Weather Research and Forecasting (WRF) Model in [Ying and Zhang \(2017\)](#). They found that the practical predictability limit decreases rapidly as scale decreases along with many other interesting error analysis and results about the predictability. More specifically, one of the conclusions in [Ying and Zhang \(2017\)](#) is that precipitation has a more limited predictability in comparison to other variables, and its practical predictability limit is only 3 days for large scales and < 12 h for the smaller scales. Both the decreasing predictability for smaller scales and the limited predictability of precipitation are also reflected in the present paper to some extent. In other work, [Neena et al. \(2014\)](#) estimate MJO predictability to be 20-30 days based on single-member hindcast and 35-45 days based on ensemble-mean hindcasts, respectively. Those results are somewhat consistent with the 20-30-day predictability of the MJO estimated in the present paper, although it is difficult to compare in detail due to the different quantities predicted. [Neena et al. \(2014\)](#) focus on predictions of the real-time multivariate (RMM) MJO index of [Wheeler and Hendon \(2004\)](#), which is based on zonal winds and OLR, variables that are typically seen to be more predictable than precipitation, which was the variable of focus in the present paper. Beyond these examples of prior work, there are also a number of other interesting papers that examine the practical predictability of current models (e.g., [Wheeler et al., 2017](#); [Kim et al., 2018](#); [Vitart and Robertson, 2018](#), and references therein).

7 Conclusion

In this paper, the main goal was to analyze the predictability of CCEWs and the MJO, and to assess how important each wave type is to the predictability of the full rainfall signal. The methodology utilized observational data as much as possible, in order to avoid the influence of any particular model's assumptions about detailed physics parameterizations. Also, the methodology allowed the forecasts to be decomposed into the contributions from each wave type (CCEWs, the MJO, and a background spectrum or non-wave component), and each wave type was treated with an independent forecast model. In this way, one wave type could be considered by itself in isolation, or one wave type could be excluded to measure its influence on the full rainfall signal.

CCEWs and the MJO were seen to provide a significant source of predictability. If the tropics had no CCEWs nor MJO, then it would arguably be a tropics where the entire spectrum looks like the non-wave component, or background spectrum or random scattered thunderstorms (e.g., [Hottovy and Stechmann, 2015](#)). Since the non-wave component of rainfall has a predictability of 0 to 3 days, whereas the the overall predictability of tropical rainfall was estimated to be roughly 3 to 6 days, over the Indian and Pacific Ocean regions, one could say that CCEWs and the MJO contribute approximately 3 additional days of predictability. From a slightly different viewpoint, one could say that CCEWs and the MJO double the range of predictability, from 0-3 days to 3-6 days. These results help to quantify the importance of CCEWs and the MJO, in terms of rainfall predictability, as an alternative measure of importance beyond more traditional measures such as climatological variance (e.g., [Takayabu, 1994a,b](#); [Wheeler and Kiladis, 1999](#)).

Two factors are perhaps sufficient to explain the importance of each wave type: decorrelation time and variance. For the first factor, if a wave type has a long decorrelation time, then it is also likely to be predictable at long lead times. For the second factor, if a wave type has a large variance—i.e., if it contributes a significant fraction of the overall

variance—then it is likely to make a significant contribution to the overall predictability as well. In the case of the non-wave component, which has largest contribution to variance of all mode types, the contribution is to limit the overall predictability to several days, in opposition to the other wave types, such as the MJO, which are more predictable but which have lesser contributions to the overall variance. The wave-exclusion studies of section 4 helped to quantify the contributions of each wave type, and to illustrate the importance of the two factors of decorrelation time and variance.

In a comparison of two datasets, OLR data was seen to be much more predictable than TRMM precipitation data. Such a result is consistent with the well-known general property that OLR data is more smoothly varying in space and time than precipitation data. Here a quantitative comparison was given in terms of predictability. OLR was seen to be more predictable than rainfall, over many locations in the Indian and Pacific Ocean regions, by approximately 5 to 10 days. Given that rainfall predictability was estimated to be roughly 3 to 6 days, the additional predictability of 5 to 10 days for OLR is quite large. One implication is that it could be difficult to compare and contrast different studies, such as [Dias et al. \(2018\)](#) who analyzed precipitation and [Janiga et al. \(2018\)](#) who analyzed OLR.

Finally, results were also provided for another question: What are the decay time scales of CCEWs and the MJO? Observational estimates of the decay time scales were provided here in Table 1, and they can be compared with the decay time scales predicted by theoretical models (e.g., [Stechmann and Hottovy, 2017](#); [Ogrosky et al., 2019](#)). As a brief comparison, [Stechmann and Hottovy \(2017\)](#) report theoretical values of MJO decay time scales of roughly 1.5 months in their standard parameter regime. Here the MJO decay time scale was estimated from precipitation observations to be roughly 3 months. Note, however, that the 3-month estimate was based on fitting the autocorrelation function for lags of roughly 0 to 30 days (in order to provide an accurate forecast for these relatively short lag times). Instead, if the autocorrelation function were fit for longer lags, such as 0 to 100 days (see Fig. 1a,d), then an estimate of roughly 1.5 months would be more appropriate, based on the decay of the autocorrelation function from lag 0 to a lag of 50 or 100 days. As another estimate, if OLR is used instead of precipitation data, we found decay times of roughly 1.7 months for zonal wavenumbers 1, 2, and 3. In brief, while different methods could lead to different decay time scales from observational estimates, and while different parameter values could lead to different decay time scales from theoretical models, there is some broad agreement between observations and theory in this preliminary comparison. It would be interesting in the future to make a more detailed comparison between theoretical and observational estimates of CCEW and MJO decay time scales.

Acknowledgements

The authors thank Andreas Schlueter and an anonymous reviewer for helpful comments. The research of S.N.S. is partially supported by a Sloan Research Fellowship from the Alfred P. Sloan Foundation and a Vilas Associates Award from the University of Wisconsin-Madison Office of the Vice Chancellor for Research and Graduate Education with funding from the Wisconsin Alumni Research Foundation.

Supporting Information

Figure S1: Estimated frequency $|\hat{\omega}|$ (CPD) for different wave types

Figure S2: Decreased forecast skill in terms of percentage of the full prediction skill in wave exclusion tests

Figure S3: Stacked variance of MJO, ER, Kelvin and Non-wave Component

References

- Chen, N. and Majda, A. J. (2015) Predicting the real-time multivariate madden–julian oscillation index through a low-order nonlinear stochastic model. *Mon. Wea. Rev.*, **143**, 2148–2169.
- Chen, N., Majda, A. J. and Giannakis, D. (2014) Predicting the cloud patterns of the Madden–Julian Oscillation through a low-order nonlinear stochastic model. *Geophys. Res. Lett.*, **41**, 5612–5619.
- Dias, J., Gehne, M., Kiladis, G. N., Sakaeda, N., Bechtold, P. and Haiden, T. (2018) Equatorial waves and the skill of NCEP and ECMWF numerical weather prediction systems. *Mon. Wea. Rev.*, **146**, 1763–1784.
- Gardiner, C. W. (2004) *Handbook of stochastic methods: for physics, chemistry & the natural sciences*, vol. 13 of *Springer Series in Synergetics*. Springer–Verlag, Berlin.
- Hottovy, S. and Stechmann, S. N. (2015) A spatiotemporal stochastic model for tropical precipitation and water vapor dynamics. *J. Atmos. Sci.*, **72**, 4721–4738.
- Hung, M.-P., Lin, J.-L., Wang, W., Kim, D., Shinoda, T. and Weaver, S. J. (2013) MJO and convectively coupled equatorial waves simulated by CMIP5 climate models. *J. Climate*, **26**, 6185–6214.
- Janiga, M., Schreck, C., JA, R., Flatau, M., Barton, N., Metzger, E. and Reynolds, C. (2018) Subseasonal forecasts of convectively coupled equatorial waves and the mjo: activity and predictive skill. *Monthly Weather Review*, **146**, 2337–2360.
- Jiang, X., Waliser, D. E., Xavier, P. K., Petch, J., Klingaman, N. P., Woolnough, S. J., Guan, B., Bellon, G., Crueger, T., DeMott, C. et al. (2015) Vertical structure and physical processes of the Madden–Julian oscillation: Exploring key model physics in climate simulations. *Journal of Geophysical Research: Atmospheres*, **120**, 4718–4748.
- Kiladis, G. N., Dias, J., Straub, K. H., Wheeler, M. C., Tulich, S. N., Kikuchi, K., Weickmann, K. M. and Ventrice, M. J. (2014) A comparison of OLR and circulation-based indices for tracking the MJO. *Mon. Wea. Rev.*, **142**, 1697–1715.
- Kiladis, G. N., Wheeler, M. C., Haertel, P. T., Straub, K. H. and Roundy, P. E. (2009) Convectively coupled equatorial waves. *Rev. Geophys.*, **47**, RG2003.
- Kim, H.-M., Vitart, F. and Waliser, D. E. (2018) Prediction of the madden–julian oscillation: A review. *J. Climate*, **31**, 9425–9443.
- Lau, W. K. M. and Waliser, D. E. (eds.) (2012) *Intraseasonal Variability in the Atmosphere–Ocean Climate System*. Springer, Berlin, 2nd edn.
- Li, Y. and Stechmann, S. N. (2018) Spatial and temporal averaging windows and their impact on forecasting: exactly solvable examples. *Math. Clim. Weather Forecast.*, **4**, 23–49.
- Liebmann, B. and Smith, C. A. (1996) Description of a complete (interpolated) outgoing longwave radiation dataset. *Bull. Amer. Meteor. Soc.*, **77**, 1275–1277.
- Lin, J.-L., Kiladis, G. N., Mapes, B. E., Weickmann, K. M., Sperber, K. R., Lin, W., Wheeler, M., Schubert, S. D., Del Genio, A., Donner, L. J., Emori, S., Gueremy, J.-F., Hourdin, F., Rasch, P. J., Roeckner, E. and Scinocca, J. F. (2006) Tropical intraseasonal variability in 14 IPCC AR4 climate models Part I: Convective signals. *J. Climate*, **19**, 2665–2690.
- Lorenz, E. N. (1969) Atmospheric predictability as revealed by naturally occurring analogues. *Journal of the Atmospheric Sciences*, **26**, 636–646.
- (1982) Atmospheric predictability experiments with a large numerical mode. *Tellus*, **34**, 505–513.
- (1996) Predictability—a problem partly solved. *Proc. Seminar on Predictability, Reading, United Kingdom*, ECMWF, 1–18.
- Majda, A., Timofeyev, I. and Vanden Eijnden, E. (2001) A mathematical framework for stochastic climate models. *Communications on Pure and Applied Mathematics*, **54**, 891–974.

- Majda, A. J. and Harlim, J. (2012) *Filtering Turbulent Complex Systems*. Cambridge University Press.
- Neena, J. M., Lee, J. Y., Waliser, D., Wang, B. and Jiang, X. (2014) Predictability of the Madden–Julian oscillation in the intraseasonal variability hindcast experiment (ISVHE). *J. Climate*, **27**, 4531–4543.
- Ogrosky, H. R. and Stechmann, S. N. (2015a) Assessing the equatorial long-wave approximation: asymptotics and observational data analysis. *J. Atmos. Sci.*, **72**, 4821–4843.
- (2015b) The MJO skeleton model with observation-based background state and forcing. *Q. J. Roy. Meteor. Soc.*, **141**, 2654–2669.
- (2016) Identifying convectively coupled equatorial waves using theoretical wave eigenvectors. *Mon. Wea. Rev.*, **144**, 2235–2264.
- Ogrosky, H. R., Stechmann, S. N. and Hottovy, S. (2019) Instability and nonlinear evolution of the MJO in a tropical channel model with vertically-varying convective adjustment. *Theor. Comp. Fluid Dyn.*, in press.
- Ogrosky, H. R., Stechmann, S. N. and Majda, A. J. (2017) Boreal summer intraseasonal oscillations in the MJO skeleton model with observation-based forcing. *Dyn. Atmos. Oceans*, **78**, 38–56.
- Stechmann, S. N. and Hottovy, S. (2017) Unified spectrum of tropical rainfall and waves in a simple stochastic model. *Geophys. Res. Lett.*, **44**, 10,713–10,724.
- Stechmann, S. N. and Majda, A. J. (2015) Identifying the skeleton of the Madden–Julian oscillation in observational data. *Mon. Wea. Rev.*, **143**, 395–416.
- Stechmann, S. N. and Ogrosky, H. R. (2014) The Walker circulation, diabatic heating, and outgoing longwave radiation. *Geophys. Res. Lett.*, **41**, 9097–9105.
- Sun, Y. Q. and Zhang, F. (2016) Intrinsic versus practical limits of atmospheric predictability and the significance of the butterfly effect. *Journal of the Atmospheric Sciences*, **73**, 1419–1438.
- Takayabu, Y. N. (1994a) Large-scale cloud disturbances associated with equatorial waves. I: Spectral features of the cloud disturbances. *J. Meteor. Soc. Japan*, **72**, 433–449.
- (1994b) Large-scale cloud disturbances associated with equatorial waves. II: Westward-propagating inertio-gravity waves. *J. Meteor. Soc. Japan*, **72**, 451–465.
- Vitart, F. and Robertson, A. W. (2018) The sub-seasonal to seasonal prediction project (s2s) and the prediction of extreme events. *npj Climate and Atmospheric Science*, **1**, 3549.
- Waliser, D. (2012) Predictability and forecasting. In *Intraseasonal Variability in the Atmosphere–Ocean Climate System* (eds. W. K. M. Lau and D. E. Waliser). Springer, Berlin.
- Wheeler, M. and Kiladis, G. N. (1999) Convectively coupled equatorial waves: analysis of clouds and temperature in the wavenumber–frequency domain. *J. Atmos. Sci.*, **56**, 374–399.
- Wheeler, M. and Weickmann, K. M. (2001) Real-time monitoring and prediction of modes of coherent synoptic to intraseasonal tropical variability. *Mon. Wea. Rev.*, **129**, 2677–2694.
- Wheeler, M. C. and Hendon, H. H. (2004) An all-season real-time multivariate MJO index: Development of an index for monitoring and prediction. *Mon. Wea. Rev.*, **132**, 1917–1932.
- Wheeler, M. C., Zhu, H., Sobel, A. H., Hudson, D. and Vitart, F. (2017) Seamless precipitation prediction skill comparison between two global models. *Q.J.R. Meteorol. Soc.*, **143**, 374–383.

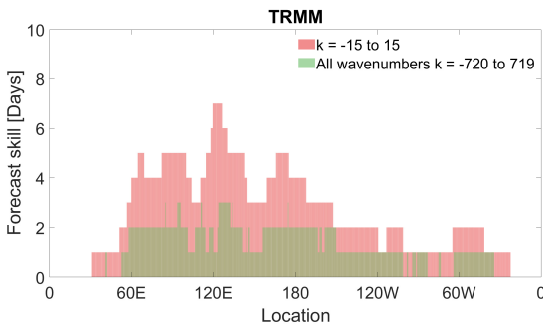
Ying, Y. and Zhang, F. (2017) Practical and intrinsic predictability of multiscale weather and convectively coupled equatorial waves during the active phase of an mjo. *J. Atmos. Sci.*, **74**, 3771–3785.

Zhang, F., A. M. O. and Nielsen-Gammon, J. W. (2006) Mesoscale predictability of an extreme warm-season precipitation event. *Wea. Forecasting*, **21**, 149–166.

Zhang, C. (2005) Madden–Julian Oscillation. *Rev. Geophys.*, **43**, RG2003.

Zhang, F., N. B. R. R. C. S. and Epifanio, C. C. (2007) Mesoscale predictability of moist baroclinic waves: Convectionpermitting experiments and multistage error growth dynamics. *Journal of the Atmospheric Sciences*, **64**, 3579–3594.

8 graphical abstract



The intrinsic predictability of tropical rainfall is estimated through several potential sources of predictability, including the convectively coupled equatorial waves (CCEWs) and Madden-Julian Oscillation (MJO), using mainly observational TRMM (Tropical Rainfall Measuring Mission) data here. In summary, no single wave type dominates the predictability of tropical rainfall; each of the mode types (MJO, CCEWs, and the background spectrum or non-wave component) has an appreciable contribution, due to variance contribution, length of decorrelation time, or a combination of these factors.

The intrinsic predictability of tropical rainfall is estimated through several potential sources of predictability, including the convectively coupled equatorial waves (CCEWs) and Madden-Julian Oscillation (MJO), using mainly observational TRMM (Tropical Rainfall Measuring Mission) data here. In summary, no single wave type dominates the predictability of tropical rainfall; each of the mode types (MJO, CCEWs, and the background spectrum or non-wave component) has an appreciable contribution, due to variance contribution, length of decorrelation time, or a combination of these factors.